# An Early Holocene primary proto-dolomite layer of abiotic origin in Lake Sayram, Central Asia

**Jianru Cheng[1], Xianqiang Meng[2*], Enlou Zhang[2], Qingfeng Jiang[3*], Zhenyu Ni[2], Junfeng Ji[1]**

Ministry of Education Key Laboratory of Surficial Geochemistry, School of Earth Sciences and Engineering, Nanjing
University, Nanjing, China,
Ministry of Education Key Laboratory of Surficial Geochemistry, School of Earth Sciences and Engineering, Nanjing
University, Nanjing, China,
Ministry of Education Key Laboratory of Surficial Geochemistry, School of Earth Sciences and Engineering, Nanjing
University, Nanjing, China,

[1]Ministry of Education Key Laboratory of Surficial Geochemistry, School of Earth Sciences and Engineering, Nanjing University, Nanjing, China.

[2]State Key Laboratory of Lake Science and Environment, Nanjing Institute of Geography and Limnology, Chinese Academy of Sciences, Nanjing, China.

[3]School of Geography Sciences, Nantong University, Nantong, China.

*Corresponding author: X. Meng (xqmeng@niglas.ac.cn) and Q. Jiang (qfjiangz@ntu.edu.cn)

**Key Points**

- An Early Holocene lacustrine proto-dolomite layer was reported, whose mean proto-dolomite content is >50 wt%.

- Morphologic and stable isotopic features distinguish these proto-dolomites from detrital dolomites and further support their abiotic origin.

- The precursor to proto-dolomite is high-Mg calcite or disordered dolomite, which favors previous empirical studies.

3

**Abstract**

The "dolomite problem" is a long-standing puzzle in sedimentology and mineralogy. Previous studies have shown that some dolostones are formed by microbes or in hydrothermal-burial environments. Here, we provide a different case in which an abiotic and Ca-rich proto-dolomite layer with weak cation ordering precipitated in Lake Sayram, Central Asia, during the Early Holocene. The 12-cm-thick layer, with abundant proto-dolomite (mean>50 wt% and maximum=81 wt%), consists of euhedral and rhombohedral grains. The similar $\delta^{18}O$ values of proto-dolomites and ostracods at the same depth demonstrate that the former are authigenic. Morphologic and isotopic features of these proto-dolomites are distinct from those of microbial dolomites, suggesting an abiotic origin. We infer that this proto-dolomite layer is the product of a warming and arid climate, which is supported by regional climatic records. This study provides evidence for previous studies that dolomite can precipitate directly in "dolomite seas" at ambient temperature.

**Plain Language Summary**

Dolostone is common in ancient rocks but rare in Cenozoic marine sediments, and dolomite is notoriously difficult to synthesize without microbes at room temperature; this is known as the "dolomite problem". In many studies, microbes have often been associated with dolostones, and synthesis by microbial mediation has succeeded. However, the composition and cation ordering of microbial dolomites have been questioned for the formation of dolostones. In addition, not every massive dolostones have been found with microbial structures. Hydrothermal-burial alteration is another promising solution, but recent studies have demonstrated that dolostones could also form at surface temperatures (<60°C). In this study, we investigated a Holocene lacustrine proto-dolomite layer (12-cm-thick) precipitated without microbes or burial alteration. Our results demonstrated that these proto-dolomites have low cation ordering, euhedral crystals and oxygen isotopes, similar to ostracods in the same horizon, suggesting an authigenic or penecontemporaneous origin. These euhedral and rhombic proto-dolomite grains are consistent with dolomite precipitated abiotically

54  rather than by microbial mediation. We inferred this proto-dolomite layer to be the result of local

55  warming and aridification. This study provides evidence that proto-dolomite, as a precursor of

56  dolomite, can precipitate at ambient temperatures.

57  **Key Words**

58  Proto-dolomite; Central Asia; Early Holocene; Lake sediment

59

60

**1 Introduction**

Dolomites and massive dolostones (>50 dolomite mol%) are common in ancient sedimentary rocks but rare in Quaternary marine sediments, although modern seawater is saturated with dolomite (A. Mckenzie & Vasconcelos, 2009). In addition, inorganic synthesis experiments at room temperature have failed (Land, 1998). These issues define the "dolomite problem", a long-standing mystery in sedimentology and mineralogy (Land, 1998; Vasconcelos et al., 1995; Wright & Wacey, 2005; Zhang et al., 2015).

Numerous field and laboratory studies have focused on the "dolomite problem". Some hydrothermal and burial environments can form dolostones, and many high-temperature synthesis experiments have succeeded (Arvidson & Mackenzie, 1996; Graf & Goldsmith, 1956; Kaczmarek & Sibley, 2007; Vandeginste et al., 2019) because high temperatures can lower the strong hydration enthalpy of magnesium ions and the huge energy barrier inhibiting long-range cation ordering (Warren, 2000). Nonetheless, evidence derived from petrographic observations and clumped isotope thermometers have indicated that some massive dolostones could form at Earth surface temperatures (Chang et al., 2020 and references therein). Therefore, several classic models for the formation of dolomites under ambient conditions, including the sabkha model (Shinn et al., 1965), the low-$SO_4^{2-}$ model (Baker & Kastner, 1981), the mixing-zone model (Magaritz et al., 1980), the reflux model (Adams & Rhodes, 1960), and organogenesis (Vasconcelos et al., 1995), have been presented. Among these models, organogenesis, in which microbial activities and/or secretions mediate the nucleation and growth of dolomite, prevails (A. Kenward et al., 2013; Perri et al., 2018; Sánchez-Román et al., 2009; Vasconcelos et al., 1995; Warthmann et al., 2000; Wright & Wacey, 2005; Zhang et al., 2015). However, a reexamination of many published microbial dolomites revealed that they are high-magnesium calcite (HMC) (Gregg et al., 2015). Neither the thickness nor the area of these microbial 'dolomites' reached the grade of dolostone (Ning et al., 2020), and how much

85  microbes contributed to ancient dolomite formation has been questioned (Petrash et al., 2017). In

86  contrast, several studies have suggested that massive dolostones could form with weak or no

87  microbial activity, although forming dolostones abiotically at room temperature has proven difficult

88  (Land, 1998). For example, water-level fluctuations have been identified within dolostone

89  successions (Lumsden & Caudle, 2001; Ning et al., 2020; Wang et al., 2018), and primary dolomites

90  precipitated directly in the Ediacaran "dolomite ocean" (Hood et al., 2011; Wang et al., 2020).

91  However, the specific conditions of dolomite precipitation remain ambiguous, and laboratory

92  simulations cannot fully replicate natural environments. Therefore, it is necessary to scrutinize

93  modern and Holocene dolomites and their formation environments.

94  Holocene and modern lake sediments are ideal archives to study the "dolomite problem" due

95  to their various hydrochemical conditions and lack of diagenesis. Many lakes, lagoons, and playas

96  worldwide precipitate primary dolomites (compiled in Figure S1a), but few of these dolomites are of

97  abiotic origin or have a high dolomite concentration (Last, 1990). Here, we examined early Holocene

98  sediments containing a 12-cm proto-dolomite layer collected from Lake Sayram, an alpine lake

99  located in Central Asia, to study the properties of these proto-dolomites and to explore possible

100  formation mechanisms. By combining morphological, mineralogical and isotopic methods, we

101  confirmed a primary and abiotic origin of this proto-dolomite layer with an average dolomite

102  concentration of >50 wt%. Furthermore, comparing these data with regional climate records, we

103  constrained the formation conditions of the proto-dolomite layer.

104  **2 Materials and Methods**

105  Lake Sayram (44°30′ to 44°42′N, 81°05′ to 81°15′E) is situated in Central Asia, covers an area

106  of 453 km$^2$ and has an elevation of 2071.9 m above sea level (Figure 1b). It has an average water

107  depth of 46.4 m, a maximum depth of ~99 m (in 2017), and mean annual precipitation and

108  evaporation of 350 mm and 550 mm, respectively (Jiang et al., 2013). The modern lake water is

109  saturated with dolomite, aragonite, and calcite based on hydrochemical data of surface water in 2017

110 (Table S1).

111       In July 2009, we drilled a 300-cm-long sediment core that covers the entire Holocene and the

112 late last glacial period from the center of Lake Sayram (44°34′59.0″N, 81°09′12.3″E) at a water

113 depth of 86.0 m (Figure S1c). In this study, the interval of 200-300 cm was selected, and radiocarbon

114 dating of bulk organic matter using accelerator mass spectrometry (AMS) with carbon reservoir

115 calibration was performed (Jiang et al., 2020; Jiang et al., 2013). The samples in the interval of 200-

116 300 cm were subjected to mineralogical and geochemical measurements, such as Fourier transform

117 infrared spectrophotometry (FTIR), X-ray diffraction (XRD), stable isotope composition analysis,

118 and scanning electron microscopy (SEM). Shells of *Limnocythere inopinata* (ostracods) were picked

119 out due to their abundant distribution in the core.

120       Mineral compositions were examined by XRD (Bruker D2 PHASER X, Cu-Kα, $0.02°$ $s^{-1}$). All

121 spectrograms were corrected to a sharp quartz peak at 3.345 Å. Minerals were identified by

122 characteristic diffraction peaks with JADE software. We calculated $CaCO_3$ mol% in dolomites with

123 Lumsden's equation, $N(CaCO_3)=333.33d_{104}-911.99$ (Lumsden, 1979), and cation ordering indices

124 were defined as $I_{015}/I_{110}$ (Gregg et al., 2015). Using TOPAS 6.0 software, we semi-quantified the ratio

125 of carbonate mineral phases (dolomite, calcite and aragonite) with Rietveld refinements to prepare

126 for the following FTIR quantification. Clay minerals in surface deposits were examined with XRD

127 after preparation of oriented clay mounts (Dohrmann et al., 2009).

128       Quantitative analyses of total carbonates were conducted with a Thermo Nicolet 6700 FTIR

129 equipped with a diffuse reflectance attachment. Total carbonate displays a wide band approximately

130 2513 $cm^{-1}$. Following the instructions of Ji et al. (2009) and Meng et al. (2015), we obtained absolute

131 mass fractions of total carbonate with external calibration. Subsequently, we calculated the dolomite,

132 calcite and aragonite contents based on carbonated mineral phases derived from XRD. In addition,

133 dust from the Taklimakan Desert and fluvial deposits were also processed to examine the existence

134 of dolomite by peaks at 728 $cm^{-1}$.

135   Observations on the external morphology and internal microstructure were processed as

136 follows. Samples were coated with platinum and then conducted with a Zeiss Sigma 500 FE-SEM

137 equipped with energy dispersive X-ray spectroscopy. A specimen from the depth of 232 cm was

138 pasted onto copper grids and milled to thinner than 70 nm with a focused ion beam (FIB).

139 Microstructures were revealed by selected-area electron diffraction (SAED) patterns parallel to the

140 [010]-zone axis via transmission electron spectroscopy (TEM) with an FEI Tecnai F20 TEM. High-

141 resolution TEM (HRTEM) images and [010]-zone axis fast Fourier transformation (FFT) patterns

142 were also processed to obtain superlattice information.

143   Geochemical analysis was conducted on dolomite-rich samples, bulk carbonates, and ostracod

144 shells. Dolomite-rich samples (15 samples from the 222-250 cm interval) were soaked in 0.5 M

145 acetic acid for 4 hours at room temperature to remove other carbonate minerals (Yang et al., 2000).

146 Then, FTIR was used again to ensure complete removal of calcite and aragonite. For stable carbon

147 and oxygen isotope analyses, ~1 mg bulk samples, dolomite-rich samples and ostracods were

148 transformed to $CO_2$ by reaction with four drops of 100% phosphoric acid at 70°C. Then, $CO_2$ gases

149 were tested for $\delta^{13}C$ and $\delta^{18}O$ using a Delta plus XP IR-MS with GasBench II attachment. The $\delta^{13}C$

150 and $\delta^{18}O$ data for all samples are reported relative to the Vienna Pee Dee Belemnite (VPDB)

151 standard, and the precision is less than 0.11‰ (1σ) for $\delta^{13}C$ and 0.10‰ (1σ) for $\delta^{18}O$. The contents of

152 bulk trace elements, including Mn, Sr, and Ti, were tested with inductively coupled plasma-optical

153 emission spectrometry (ICP-OES) after digestion.
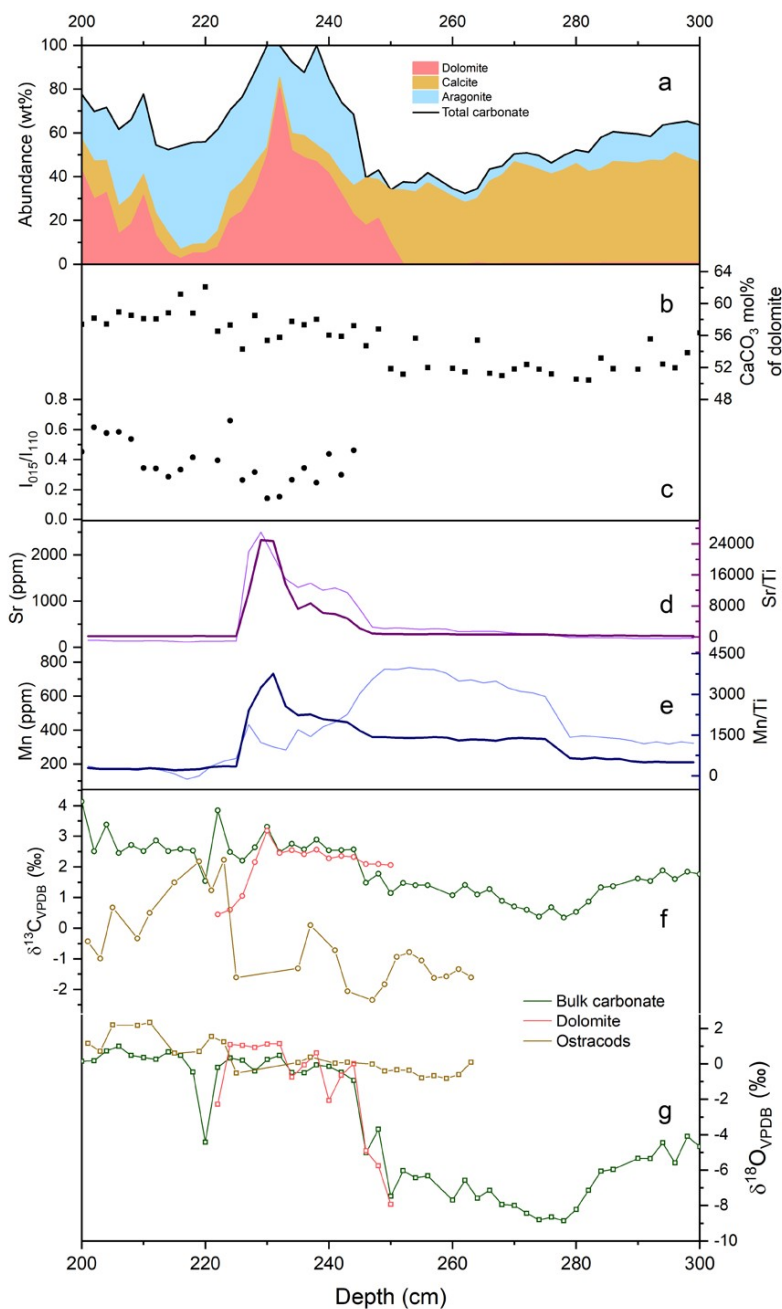
154 **3 Results**

155   Dolomites exist in almost every sample but account for the majority of the sample only in the

156 interval of 228~240 cm (the mean is greater than 50 wt%), even reaching more than 80 wt% at 232

157 cm (Figure 1a and Table S3). Dolomites in this interval have low-medium cation ordering indices

158 (<0.7), a $CaCO_3$ mol% of approximately 53% (Figure 1b and Figure 1c), and are euhedral and

159 interpenetrating rhombs (Figure 2d, 2e, 2f and Figure S2b), which are similar to the properties of

160   proto-dolomites (Gregg et al., 2015). These proto-dolomites are integrated and are independent of

161   any microbial structures, such as mycelium or bacterial cells (Samylina et al., 2016). We did not

162   find microbe-related products, including framboidal pyrite (Deng et al., 2010). The TEM bright

163   field image (Figure S4a) illustrates that smaller rhombic crystals (~200 nm) are wrapped in larger

164   crystals (~2 μm), and their orientations are different. The [010]-zone axis SAED of larger crystals

165   (Figure S4b) reveal no superstructure reflections, such as (003) (Hobbs & Xu, 2020; Lu et al.,

166   2018), the same result is shown by the HRTEM image of smaller crystals (Figure S4c) and [010]-

167   zone axis FFT patterns (Figure S4d). Therefore, we call the 228~240 cm interval the "proto-

168   dolomite layer". The $\delta^{13}C$ and $\delta^{18}O$ values of samples from the layer range from 2.15‰ to 3.18‰

169   (n=7, mean=2.51‰) and from -2.07‰ to 1.14‰ (n=7, mean=0.13‰), respectively (Figure 1f,

170   Figure 1g, Figure 3 and Table S4). The $\delta^{13}C$ and $\delta^{18}O$ values of ostracods are close to those of the

171   proto-dolomite layer (Figure 1f, Figure 1g, Figure 3 and Table S4). The manganese concentration

172   decreases significantly in the proto-dolomite layer, while the strontium concentration increases

173   from ~400 ppm to ~2700 ppm (the thinner lines in Figure 1d and e). After normalization to Ti, both

174   Mn and Sr increase in the proto-dolomite layer (the thicker lines in Figure 1d and e). In addition,

175   dissolution of aragonite was observed in the 232 cm sample (Figure S2b).

176        Beneath the proto-dolomite layer (242~300 cm), detrital calcite, quartz and clay minerals are

177   common (Figure S2). The calcite shows signs of transportation, such as corroded margins and etch

178   pits. The $\delta^{13}C$ and $\delta^{18}O$ values of ostracods range from -1.7‰ to 0.9‰ (n=7, mean=-1.28‰) and

179   from -0.8‰ to 0.1‰ (n=7, mean=-0.4‰), respectively (Figure 1, Figure 3 and Table S4). In contrast,

180   bulk carbonate has more positive $\delta^{13}C$ values ranging from 0.39‰ to 1.9‰ (n=23, mean=1.2‰), and

181   obvious negative $\delta^{18}O$ values ranging from -8.9‰ to -4.01‰ (n=23, mean=-6.8‰) (Figure 1 and

182   Table S4). The Sr concentration remains steady at ~200 ppm, and the Mn concentration increases

183   from ~350 ppm to ~600 ppm at the depth of approximately 277 cm (Figure 1d and 1e).

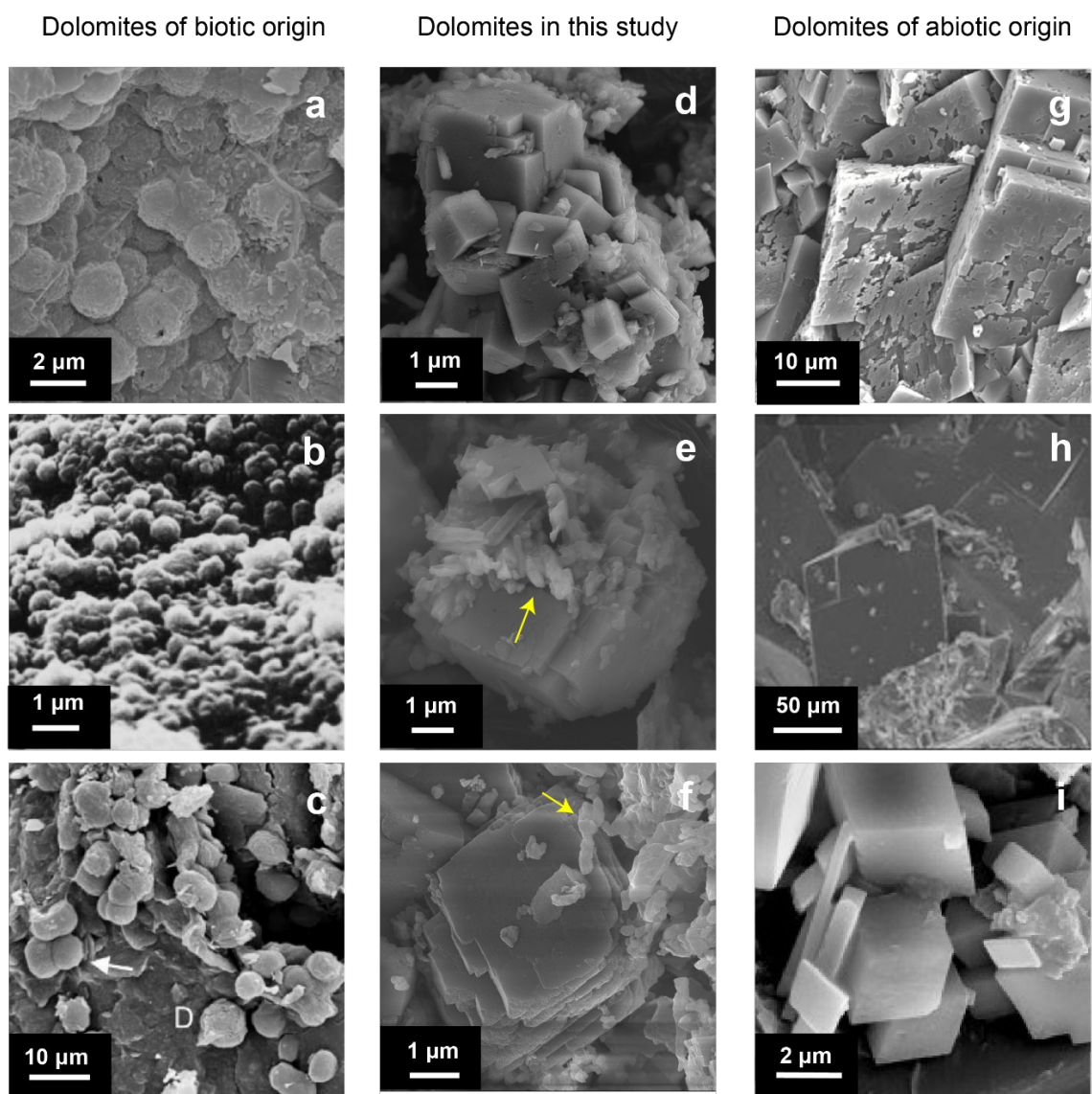184        Above the proto-dolomite layer (200~226 cm), needle-like aragonites are prevalent, and

calcites with dissolved edges compose a tiny part. Gypsum appears as tabular aggregates at a depth

of 216 cm (Figure S2). Both bulk carbonate and ostracods have similar $\delta^{18}O$ values, with an average

of 0.5‰. However, $\delta^{13}C$ is more positive in bulk carbonate (from 2.5‰ to 4.1‰, n=10, mean=2.7‰)

than in ostracods (from 0.6‰ to 2.3‰, n=7, mean=1.4‰) (Figure 1, Figure 3 and Table S4). Mn and

Sr concentrations decrease to the previous 280-300 cm levels.



**Figure 1.** Mineralogical and geochemical compositions within the 200-300 cm interval of the core

192    from Lake Sayram. **(a)** Overall distribution of dolomite, aragonite and calcite (bands) as well as the

193    concentration of total carbonates (black line). **(b)** $CaCO_3$ mol% in dolomites calculated with the

194    equation by Lumsden (1979). **(c)** Cation ordering (identity ratio of $d_{015}$ and $d_{110}$). Some data are

195    absent because dolomite concentrations are too low to calculate ordering. **(d)** Strontium

196    concentration (light purple line) and Sr/Ti (bold purple line). **(e)** Manganese concentration (light blue

197    line) and Mn/Ti (bold blue line). **(f)** $\delta^{13}C$ of bulk carbonate, dolomite and ostracods. **(g)** $\delta^{18}O$ of bulk

198    carbonate, dolomite and ostracods. Note that the $\delta^{18}O$ values of bulk carbonate and dolomite verge

199    on the $\delta^{18}O$ values of ostracods.

| Dolomites of biotic origin | Dolomites in this study | Dolomites of abiotic origin |
|---|---|---|

**Figure 2.** The morphologies of proto-dolomites in Lake Sayram are shown in the middle column, and for comparison, dolomites of biotic and abiotic origins are listed in the left and right columns, respectively. **(a)** Spheroidal microstructures composed of dolomite related to methanogens in Permian lake deposits (Sun et al., 2020). **(b)** Spherical modern dolomite mediated by sulfate-reducing bacteria from the Coorong area, South Australia (Borch & Jones, 1976; Wright & Wacey, 2005). **(c)** Microbial dolomites grouped in tetrads found in Miocene saline lake deposits in the Madrid Basin (Sanz-Montero et al., 2006). **(d)** Aggregates of rhombohedral proto-dolomite with

208  smooth facets in Lake Sayram (this study). **(e)** and **(f)** Proto-dolomites with smooth facets and

209  imperfect or coarse steps accompanied by dissolved aragonites (marked by yellow arrows) in Lake

210  Sayram (this study). **(g)** Ideal dolomite precipitated in the laboratory at 218°C through

211  recrystallization of calcite seeds (Kaczmarek & Sibley, 2014). **(h)** Island dolostones from the Xisha

212  Islands (Na et al., 2019) that precipitated due to sea-level changes and were modified by sea water

213  (Wang et al., 2018). **(i)** Mississippian dolostones formed within hot (170-215°C) and saline brines

214  (Kolchugin et al., 2020).

215  **4 Discussion**

216  **4.1 Abiotic origin of proto-dolomite layer** *in situ*

217      The $CaCO_3$ mol% values of ~53%, the weak but existing superstructure peaks, and local

218  disordering (Figures 1c, S2, S4 and Table S5) confirm that Lake Sayram samples from the 228-240

219  cm interval are dominated by proto-dolomites (Gregg et al., 2015; Petrash et al., 2017). Before

220  discussion of the mechanism, it is necessary to identify whether these proto-dolomites are exogenous

221  or authigenic. Exogenous materials within Lake Sayram sediments include windblown dust and

222  detritus from lake basin carried by rivers. Central Asian dust contains an average dolomite content of

223  2.2% in the bulk fraction and an average dolomite content of 4.6% in the fine-grained fraction (Meng

224  et al., 2019), and fluvial deposits contain no dolomite (Figure S3). SEM images illustrate that the

225  crystals of proto-dolomites are euhedral and rhombic (Figure 2d) and have no traces of transportation

226  or dissolution (as shown in Li et al., 2007). Furthermore, Lake Sayram proto-dolomites have $\delta^{13}C$-

227  $\delta^{18}O$ values that are different from Asian dust (Li et al., 2007) but are similar to those of ostracods

228  from the same depth (Figure 3a). According to these pieces of evidence, this proto-dolomite layer

229  does not have a detrital provenance.

230      Proto-dolomites and *L. inopinata* ostracods have similar $\delta^{18}O$ values, which suggests that they

231  precipitated in the same solution. Notably, $\delta^{18}O_{dolomite}$ values within the 244-250 cm interval change

232  positively (from -7.9‰ to 0.0‰) and are similar to $\delta^{18}O_{ostracod}$ values when the proto-dolomite

233  fraction increases (Figure 1 and Figure 3), indicating the existing contribution of dust to oxygen

234  isotopes. To estimate the detrital contribution, we suppose $\delta^{18}O_{dolomite}$ value of 250 cm (-7.9‰) as the

235  detrital endmember and $\delta^{18}O_{ostracod}$ values from near the same depth as the authigenic endmember and

236  find that a >20 wt% authigenic partition of proto-dolomite ensures a >90% authigenic contribution

237  (Table S4). Therefore, $\delta^{18}O$ values of the proto-dolomite layer can represent $\delta^{18}O$ values of missing

238  ostracods in the 240-228 cm interval (Figure 4f).

239      Based on the deduction of authigenic origin, we further discuss whether the proto-dolomites

240  are the result of primary precipitation or secondary alternation and whether they are related to

241  microbes. Hydrothermal-burial alteration can be easily ruled out because of soft mud conditions and

242  Mn/Sr ratios of <1 (Chang et al., 2020). The euhedral and rhombic proto-dolomites are comparable

243  to abiotic dolomites which were found at the sediment-water interface (McCormack et al., 2018), in

244  the high-temperature synthesis of ideal dolomite (Figure 2g) (Kaczmarek & Sibley, 2014), in island

245  dolostones (Figure 2h) (Na et al., 2019), and in Mississippian dolostones (Figure 2i) (Kolchugin et

246  al., 2020) but are not analogous to biotic spherical dolomites from saline lakes or lagoons (Figure 2a,

247  2b and 2c) (Borch & Jones, 1976; Hu et al., 2019; Sanz-Montero et al., 2006; Sun et al., 2020;

248  Wright & Wacey, 2005). No mycelium, bacteria, or other traces of microbial activities (e.g.,

249  contacting lines in Samylina et al. (2016)) are found in the Lake Sayram samples.

250      The $\delta^{13}C_{dolomite}$ values (1.5~3.8‰) further support the abiotic origin of Lake Sayram dolomite.

251  The controlling factors of $\delta^{13}C_{carbonate}$ include temperature, $\delta^{13}C_{DIC}$ of lake water, and $\delta^{13}C_{DIC}$ of pore

252  water. The effect of temperature is slight ($\Delta_{carbonate-DIC}$ decreases 0.035‰/°C at 20°C, calculated by

253  Emrich et al. (1970)), while the other two factors, which are controlled by microbial activities,

254  significantly affect $\delta^{13}C_{carbonate}$. Various biogenic or organogenic dolomites in previous studies have

255  distinct $\delta^{13}C_{dolomite}$ values compared to Lake Sayram samples (Figure 3b). For instance, $\delta^{13}C_{dolomite}$

256  ranges from -50‰ to -30‰ due to sulfate-driven anaerobic oxidation of methane (SD-AOM)

257  consortium (Lu et al., 2018), from 6‰ to 20‰ when influenced by methanogenic archaea (Sun et al.,

258  2020), from -60‰ to -40‰ when derived from methane oxidization (Aloisi et al., 2002), and from -

259  36‰ to 13‰ when precipitated on sulfate-methane interfaces (Meister et al., 2007). In addition,

260  proto-dolomites have slightly positive $\delta^{13}C$ values compared with *L. inopinata* ostracods in the proto-

261  dolomite layer, which accords with higher carbon isotope fractionation factor of dolomite-dissolved

262  inorganic carbon (DIC) than that of calcite-DIC (Li et al., 2016) and the $\Delta^{13}C_{calcite-ostracods}$ at a level of

263  1~2‰ due to vital effects (Grafenstein et al., 1999; Van der Meeren et al., 2011).

264  Briefly, this systematic investigation demonstrates that the Lake Sayram proto-dolomite layer

265  precipitated *in situ* and without involvement by microbes or hydrothermal processes.
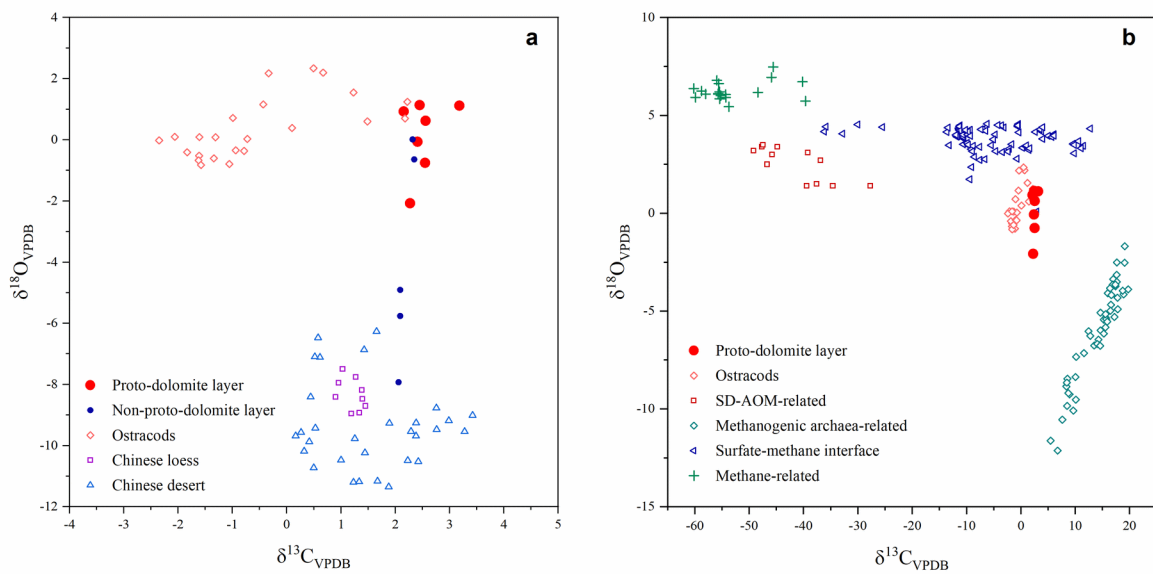


**Figure 3.** Comparison of dolomite C-O isotope compositions of Lake Sayram with other origins. **(a)**
$\delta^{13}C$-$\delta^{18}O$ cross-plot of the proto-dolomite layer, non-proto-dolomite layer and ostracods in this study
and reported potential provenances, including Chinese Loess and deserts (Li et al., 2007), Cretaceous
lacustrine dolostones from the Tianshan Mountains (Wang et al., 2020) and proto-dolomite in the
Red Clay Formation in Chinese Loess (He et al., 2012). **(b)** $\delta^{13}C$-$\delta^{18}O$ cross-plot of the proto-
dolomite layer and ostracods in this study as well as microbial dolomitization models, including
sulfate-driven anaerobic oxidation of methane consortium (Lu et al., 2018), methane generation by
archaea (Sun et al., 2020), methane oxidization (Aloisi et al., 2002), and microbial activities at the

275    sulfate-methane interface (Meister et al., 2007).

276    **4.2 Mechanism of proto-dolomite layer formation**

277    How does this proto-dolomite layer form? We address three aspects of this question: (1) What

278    is the precursor to proto-dolomite? (2) How do $Mg^{2+}$ ions dehydrate and incorporate into the

279    precursor, and how long does this process take? (3) Why did cations not reach perfect ordering?

280    The precursor to dolomite remains controversial, but several experiments have demonstrated

281    that they are a series of metastable intermediate phases, including aragonite, Mg-rich calcite,

282    hydrated Ca-Mg-carbonate, and disordered dolomite (Gregg et al., 2015). In Persian Gulf sabkhas,

283    dolomite accompanied by aragonite has drawn much attention and has led to the aragonite

284    replacement hypothesis (Brauchli et al., 2015). However, later studies revealed this mechanism to be

285    unrealistic at ambient temperature because dolomite and aragonite have distinct lattice configurations

286    (Li et al., 2015) so that the energy barrier for aragonite to convert to dolomite is too high (Brauchli et

287    al., 2015; Dunham et al., 2020). Although the dissolution of aragonite has also been observed in this

288    study (Figure 2e, 2f and Figure S2b), we do not consider aragonite as the precursor because no

289    aragonite-like pseudomorph was observed. The dissolution of aragonite may provide extra $Ca^{2+}$ ions

290    to precursors in the immediate vicinity. Very high-Mg calcite (VHMC) and disordered dolomite are

291    promising precursors found in both the field and laboratory (Dunham et al., 2020; Gregg et al., 2015;

292    Wright, 1997; Zhang et al., 2012; Zhang et al., 2015). The TEM images revealed small rhombic

293    crystals (~200 nm) inside the aggregates (Figure S4a), and whether SAED or FFT of HRTEM image

294    showed no superstructure reflections (Figure S4b, c and d). Therefore, we consider VHMC or

295    disordered dolomite to be the precursor. The extremely high $Mg^{2+}$ concentration (19.8 mmol/L) and

296    high Mg:Ca ratio (~27.5) in Lake Sayram (see Table S1) could have enabled a short induction time

297    (Hobbs & Xu, 2020; Kaczmarek & Sibley, 2011).

298    To address question (2), the rigid hydration shells around dissolved $Mg^{2+}$ ions restrict $Mg^{2+}$

299    incorporation (Lippmann, 1974), and dehydration may be the rate-limiting step in dolomite

300 precipitation at ambient temperature (Petrash et al., 2017; Shen et al., 2015). To resolve this

301 question, high-temperature water-free solutions, microbes, and catalysts were used in synthesis trials.

302 Hydrothermal-burial conditions can lower the energy barrier (Graf & Goldsmith, 1956) and microbes

303 can release carboxyl groups and polysaccharides weakening hydration shells (Brauchli et al., 2015;

304 Roberts et al., 2013; Shen et al., 2015; F. Zhang et al., 2012; Zhang et al., 2015). However, we have

305 demonstrated that the Lake Sayram proto-dolomite layer is independent of hydrothermal fluids and

306 microbial activities. Clay minerals with negative-charged surfaces, such as montmorillonite and illite

307 (Figure S5), catalyze the dehydration of $Mg^{2+}$, but they result in cauliflower- and dumbbell-shaped

308 (proto-)dolomite grains (Liu et al., 2019; Wanas & Sallam, 2016), which are not applicable to this

309 study. In addition, elements including zinc, Mn(II), and silica have been found to facilitate dolomite

310 precipitation (Daye et al., 2019; Hobbs & Xu, 2020; Vandeginste et al., 2019). Manganese increased

311 in the Lake Sayram section after normalization to Ti (Figure 1e) suggesting an increase of Mn

312 incorporation in authigenic fraction because Ti usually exists in detrital minerals, is insensitive to

313 redox conditions and difficult to dissolve (Yancheva et al., 2007). However, since the existing forms

314 of Mn are uncertain, whether and how they influenced proto-dolomite precipitation is doubtful.

315 Evaporitic environments, such as playa lakes, sabkhas, and hypersaline lagoons (Sadooni et al.,

316 2010; Wright & Wacey, 2005), and water-free solutions (Xu et al., 2013) also favor magnesium

317 dehydration, but aridity is not a sufficient condition, as proven by Land (1998).

318      An empirical study by Hobbs and Xu (2020) showed that cycles of temperature and pH in

319 solutions with high $Mg^{2+}$ concentrations and high Mg:Ca ratios facilitate the precipitation of Mg-rich

320 carbonates by promoting preferential dissolution of existing $Ca-CO_3$ bonds and later incorporation of

321 $Mg^{2+}$. This mechanism sheds light on the formation of proto-dolomite layer in Lake Sayram section.

322 According to the depth-age model established by Jiang et al. (2020), the dolomite layer formed

323 during 9.3~8.7 cal. kyr BP (Figure 4g). The regionally averaged temperature index (Zhang & Feng,

324 2018) suggests that the temperature reached a maximum during this period (Figure 4c) and had an

325  ~2000-year lag relative to the local summer insolation maximum (Figure 4a) (Laskar et al., 2004;

326  Zhao et al., 2017). Before the proto-dolomite layer formed, *Pediastrum* spp. appeared suddenly

327  (Figure 4), which demonstrates that the lake level might have shallowed to less than 15 meters (Jiang

328  et al., 2013). In agreement with previous data of moisture index in Central Asia (Figure 4d),

329  concentrations of charcoals and pollens also indicate a warm and arid climate (Figure 4h and i). On

330  the one hand, the shrinking lake had a large diel temperature range on individual days (even reaches

331  15°C) (Woolway et al., 2016) and annual maximum lake surface temperatures increases under

332  climate warming (Dokulil et al., 2021). The increase and swings of water temperature could have

333  caused iterative dissolution and precipitation, which would have favored $Mg^{2+}$ incorporation and

334  proto-dolomite growth (Hobbs & Xu, 2020). On the other hand, as the lake water concentrated, the

335  alkalinity and pH rose gradually, which favored proto-dolomite and aragonite precipitation (Figure

336  S6) (simulated after Dunham et al., 2020), and gypsum (Figure 4e) finally precipitated, coinciding

337  with an extremely high temperature (see negative PCA-2 scores in Jiang et al., 2013). High Sr

338  concentrations (>2000 ppm, Figure 1d) in the dolomite layer also support arid trends (Wang et al.,

339  2020). The partition coefficient of Sr for dolomite increases with temperature and is even higher

340  when sulfate exists (Sánchez-Román et al., 2011).

341      To address question (3), time is the crucial factor for dolomite to reach long-range cation

342  ordering. Pina et al. (2020) compiled dolomites from the Neoproterozoic to the late Holocene and

343  found that at least 30 million years are required for high ordering. XRD reveals that Lake Sayram

344  proto-dolomites have weak (015), (101), and (021) superstructure peaks (Figure S2c), indicating

345  weak ordering. The [010]-zone axis SAED results (Figure S4b) reveal no superstructure reflections,

346  such as (003) (Hobbs & Xu, 2020; Lu et al., 2018), which demonstrates that $Mg^{2+}$ and $Ca^{2+}$ are not

347  distributed in alternant layers. The HRTEM image (Figure S4c) and [010]-zone axis FFT patterns

348  (Figure S4d) also suggest a disordered distribution of cation layers. Nonstoichiometry and disorder

349  are energetic drives for proto-dolomite to recrystallize (Kaczmarek & Sibley, 2014); thus, Lake

350    Sayram proto-dolomites may reach a more perfect ordering state in the future.
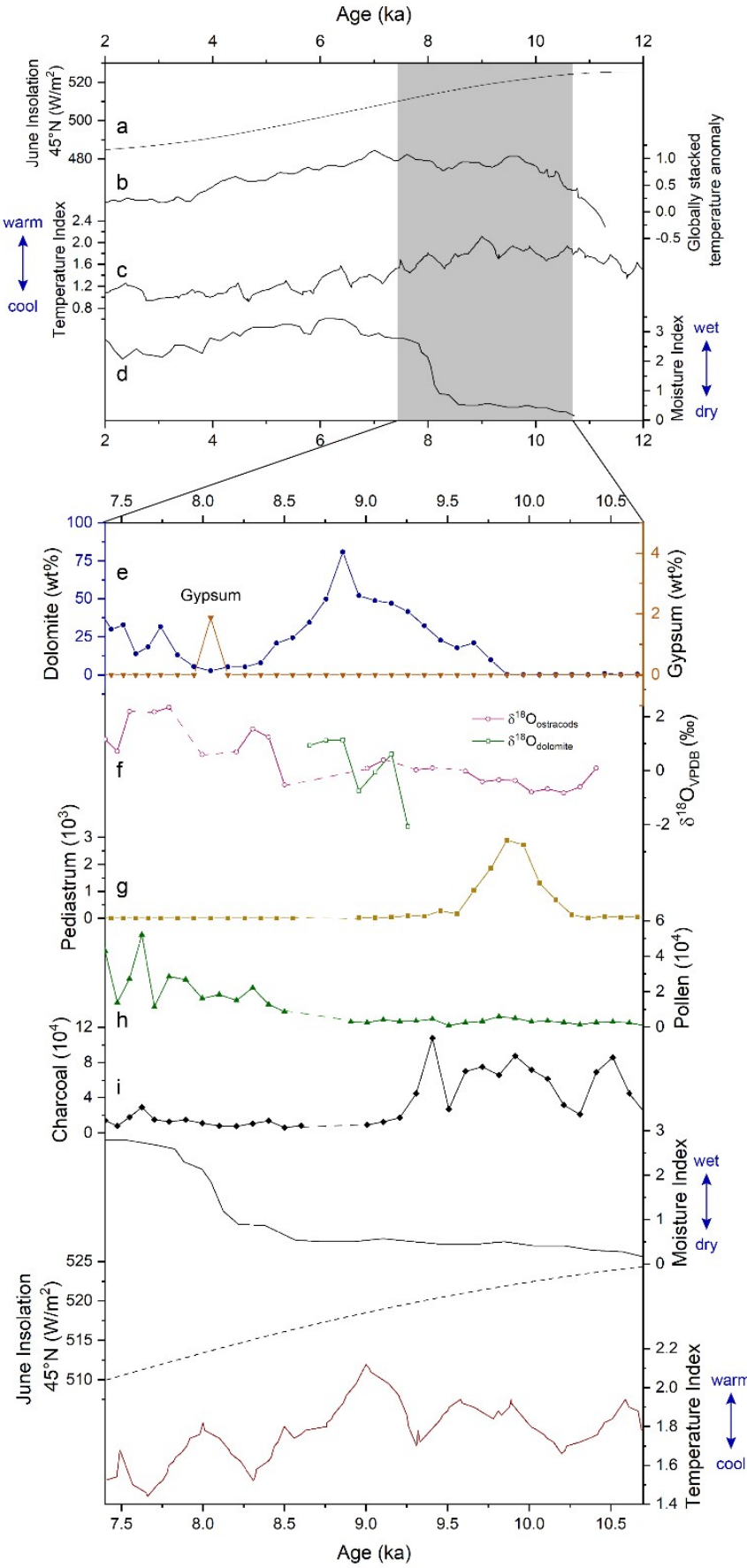
**Figure 4.** Comparison of paleoclimatic records during the period when the proto-dolomite layer formed. **(a)** Mean insolation at 45°N in June (Laskar et al., 2004). **(b)** Global stacked temperature anomaly that has increased since ~11 ka BP and maintained its maximum during ~10 - ~7 ka BP (Marcott et al., 2013). **(c)** Regionally averaged temperature index of Altai Mountain and surrounding areas that was continually warming from ~12 ka BP to ~9 ka BP and has been gradually cooling since ~9 ka BP (Zhang & Feng, 2018). **(d)** Moisture index in Central Asia indicating an extremely arid early Holocene (from ~12 ka BP to ~8 ka BP) (Chen et al., 2008). **(e)** Dolomite and gypsum concentrations vary along the section. **(g)** *Pediastrum* spp. appeared suddenly just before the proto-dolomite later formation (Jiang et al., 2013). **(h)** Increasing total pollen counts indicate that the regional climate has become wetter since ~8.5 ka BP (Jiang et al., 2013). **(i)** Charcoal counts indicate that the changing high temperatures resulted in increases in the frequency of local fires during 11.0-9.4 cal. kyr BP (Jiang et al., 2013).

**4.3 Implications for geological records and the Early Holocene climate in Central Asia**

First, this study provides a detailed investigation on primary proto-dolomite in ambient conditions and of abiotic origin during the early Holocene, supporting several studies of ancient abiotic dolostones. For example, massive dolostones in the Doushantuo Formation formed at temperatures <60°C (Chang et al., 2020), and primary dolomite could precipitate directly in "Neoproterozoic aragonite-dolomite seas" (Hood et al., 2011; Wang et al., 2020). This study also supports the viewpoint of Wang et al. (2016) that the removal of sulfate may play little role in dolomite precipitation at surface temperatures because Lake Sayram has a high sulfate concentration (~16.88 mmol/L).

Second, lacustrine dolomites may respond to regional warm and not just arid trend. The proto-dolomite layer also corresponded to a warm period both locally (Figure 4c) (Zhang & Feng, 2018) and globally (Figure 4b) (Marcott et al., 2013). A similar situation was also discovered in Lake Qinghai after the Younger Dryas (Hou et al., 2015; Liu et al., 2003). This warming trend with a high

377 dolomite concentration was supported by the kinetic model from Arvidson and Mackenzie (1996),

378 which implies that dolomites respond to relatively modest warming of surface environments. If

379 correct, under global warming, lake heatwaves will become hotter and longer (Woolway et al.,

380 2021), which may facilitate lacustrine (proto-)dolomite precipitation.

381 **5 Conclusions**

382 We report a case of an abiotic lacustrine proto-dolomite layer formed during the early

383 Holocene in Lake Sayram, Central Asia. Low ordering, euhedral and rhombohedral shapes, and $\delta^{13}$C-

384 $\delta^{18}$O values confirm that the proto-dolomites precipitated authigenically and abiotically. We suggest

385 that due to warming and evaporation, disordered dolomite crystallized as a precursor in lake water

386 with high Mg:Ca ratios and $Mg^{2+}$ concentrations. More proto-dolomite then precipitated via iterative

387 preferential dissolution and reprecipitation. The dolomite-aragonite-gypsum sequence suggests an

388 arid and warm trend in Lake Sayram during 10.0-8.0 ka BP, which correlates with regional

389 temperature and moisture indices. This study also provides insight into massive low-temperature

390 abiotic dolomites.

391 **Data Availability Statement**

392 The Supporting Information and figures are available on Mendeley Data with digital object identifier

393 10.17632/7kdw9skn7h.1.

400 **References**

401 A. Kenward, P., M. Ueshima, D. Fowle, R. Goldstein, L. Gonzalez, and J. A. Roberts (2013), *Ordered low-temperature*
402 *dolomite mediated by carboxyl-group density of microbial cell walls*, 2113-2125 pp.
403 A. Mckenzie, J., and C. Vasconcelos (2009), *Dolomite Mountains and the origin of the dolomite rock of which they*

404 *mainly consist: Historical developments and new perspectives*, 205-219 pp.

405 Adams, J. E., and M. L. Rhodes (1960), Dolomitization by Seepage Refluxion1, *AAPG Bulletin*, *44*(12), 1912-1920.

406 Aloisi, G., C. Pierre, J.-M. Rouchy, and J.-C. Faugères (2002), Isotopic evidence of methane-related diagenesis in the

407 mud volcanic sediments of the Barbados Accretionary Prism, *Continental Shelf Research*, *22*(16), 2355-2372.

408 Arvidson, R. S., and F. T. Mackenzie (1996), Tentative kinetic model for dolomite precipitation rate and its application

409 to dolomite distribution., *Aquatic Geochemistry*, *2*, 273-298.

410 Baker, P. A., and M. Kastner (1981), Constraints on the Formation of Sedimentary Dolomite, *Science*, *213*, 214-216.

411 Borch, C. C., and J. B. Jones (1976), Spherular modern dolomite from the Coorong area, South Australia, *Sedimentology*,

412 *23*(4), 587-591.

413 Brauchli, M., J. A. McKenzie, C. J. Strohmenger, F. Sadooni, C. Vasconcelos, and T. R. R. Bontognali (2015), The

414 importance of microbial mats for dolomite formation in the Dohat Faishakh sabkha, Qatar, *Carbonates and Evaporites*,

415 *31*(3), 339-345.

416 Chang, B., et al. (2020), Massive formation of early diagenetic dolomite in the Ediacaran ocean: Constraints on the

417 "dolomite problem", *Proceedings of the National Academy of Sciences*, 201916673.

418 Chen, F., et al. (2008), Holocene moisture evolution in arid central Asia and its out-of-phase relationship with Asian

419 monsoon history, *Quaternary Science Reviews*, *27*(3-4), 351-364.

420 Daye, M., J. Higgins, and T. Bosak (2019), Formation of ordered dolomite in anaerobic photosynthetic biofilms,

421 *Geology*, *47*(6), 509-512.

422 Deng, S., H. Dong, G. Lv, H. Jiang, B. Yu, and M. E. Bishop (2010), Microbial dolomite precipitation using sulfate

423 reducing and halophilic bacteria: Results from Qinghai Lake, Tibetan Plateau, NW China, *Chemical Geology*, *278*(3),

424 151-159.

425 Dohrmann, R., K. B. Rüping, M. Kleber, K. Ufer, and R. Jahn (2009), Variation of preferred orientation in oriented clay

426 mounts as a result of sample preparation and composition, *Clays and Clay Minerals*, *57*(6), 686-694.

427 Dokulil, M. T., E. de Eyto, S. C. Maberly, L. May, G. A. Weyhenmeyer, and R. I. Woolway (2021), Increasing

428 maximum lake surface temperature under climate change, *Climatic Change*, *165*(3), 56.

429 Dunham, E. C., et al. (2020), An Ecological Perspective on Dolomite Formation in Great Salt Lake, Utah, *Frontiers in*

430 *Earth Science*, *8*.

431 Emrich, K., D. H. Ehhalt, and J. C. Vogel (1970), Carbon isotope fractionation during the precipitation of calcium

432 carbonate, *Earth and Planetary Science Letters*, *8*(5), 363-371.

433 Graf, D. L., and J. R. Goldsmith (1956), Some Hydrothermal Syntheses of Dolomite and Protodolomite, *The Journal of*

434 *Geology*, *64*(2), 173-186.

435 Grafenstein, v., E. U., and T. H., P (1999), Oxygen and carbon isotopes in modern fresh-water ostracod valves: assessing

436 vital offsets and autecological effects of interest for palaeoclimate studies. , *Palaeogeography, Palaeoclimatology,*

437 *Palaeoecology*, *148(1)*, 133-152.

438 Gregg, J. M., D. L. Bish, S. E. Kaczmarek, H. G. Machel, and C. Hollis (2015), Mineralogy, nucleation and growth of

439 dolomite in the laboratory and sedimentary environment: A review, *Sedimentology*, *62*(6), 1749-1769.

440 He, T., Y. Chen, W. Balsam, X. Sheng, L. Liu, J. Chen, and J. Ji (2012), Distribution and origin of protodolomite from

441 the late Miocene-Pliocene Red Clay Formation, Chinese Loess Plateau, *Geochemistry, Geophysics, Geosystems*, *13*(6), n/

442 a-n/a.

443 Hobbs, F. W. C., and H. Xu (2020), Magnesite formation through temperature and pH cycling as a proxy for lagoon and

444 playa paleoenvironments, *Geochimica et Cosmochimica Acta*, *269*, 101-116.

445 Hood, A. v. S., M. W. Wallace, and R. N. Drysdale (2011), Neoproterozoic aragonite-dolomite seas? Widespread marine

446 dolomite precipitation in Cryogenian reef complexes, *Geology*, *39*(9), 871-874.

447 Hou, J., Y. Huang, J. Zhao, Z. Liu, S. Colman, and Z. An (2015), Large Holocene summer temperature oscillations and

448 impact on the peopling of the northeastern Tibetan Plateau, *Geophysical Research Letters*, *43*, n/a-n/a.

449 Hu, Z., W. Hu, C. Liu, F. Sun, Y. Liu, and W. Li (2019), Conservative behavior of Mg isotopes in massive dolostones:

450 From diagenesis to hydrothermal reworking, *Sedimentary Geology*, *381*, 65-75.

451 Ji, J., Y. Ge, W. Balsam, J. E. Damuth, and J. Chen (2009), Rapid identification of dolomite using a Fourier Transform

452 Infrared Spectrophotometer (FTIR): A fast method for identifying Heinrich events in IODP Site U1308, *Marine Geology*,

453 *258*(1), 60-68.

454 Jiang, Q., J. Zheng, Y. Yang, W. Zhao, and D. Ning (2020), A Persistently Increasing Precipitation Trend Through the

455 Holocene in Northwest China Recorded by Black Carbon δ13C From Sayram Lake, *Frontiers in Earth Science*, *8*.

456 Jiang, Q., J. Ji, J. Shen, R. Matsumoto, G. Tong, P. Qian, X. Ren, and D. Yan (2013), Holocene vegetational and climatic

457 variation in westerly-dominated areas of Central Asia inferred from the Sayram Lake in northern Xinjiang, China ( in

458 Chinese) *Science China Earth Sciences*, *56*(3), 339-353.

459 Kaczmarek, S. E., and D. F. Sibley (2007), A Comparison of Nanometer-Scale Growth and Dissolution Features on

460 Natural and Synthetic Dolomite Crystals: Implications for the Origin of Dolomite, *Journal of Sedimentary Research*,

461 *77*(5), 424-432.

462 Kaczmarek, S. E., and D. F. Sibley (2011), On the evolution of dolomite stoichiometry and cation order during high-

463 temperature synthesis experiments: An alternative model for the geochemical evolution of natural dolomites,

464 *Sedimentary Geology*, *240*(1), 30-40.

465 Kaczmarek, S. E., and D. F. Sibley (2014), Direct physical evidence of dolomite recrystallization, *Sedimentology*, *61*(6),
466 1862-1882.

467 Kolchugin, A., A. Immenhauser, V. Morozov, B. Walter, A. Eskin, E. Korolev, and R. Neuser (2020), A comparative
468 study of two Mississippian dolostone reservoirs in the Volga-Ural Basin, Russia, *Journal of Asian Earth Sciences*, *199*.

469 Land, L. S. (1998), Failure to Precipitate Dolomite at 25 °C fromDilute Solution Despite 1000-Fold Oversaturation
470 after32 Years, *Aquatic Geochemistry*, *4*(3), 361-368.

471 Laskar, J., P. Robutel, F. Joutel, M. Gastineau, A. Correia, and B. A. Levrard (2004), A Long-term Numerical Solution
472 for the Insolation Quantities of the Earth, *http://dx.doi.org/10.1051/0004-6361:20041335*, *428*.

473 Last, W. M. (1990), Lacustrine dolomite—an overview of modern, Holocene, and Pleistocene occurrences, *Earth-*
474 *Science Reviews*, *27*(3), 221-263.

475 Li, G., J. Chen, Y. Chen, J. Yang, J. Ji, and L. Liu (2007), Dolomite as a tracer for the source regions of Asian dust,
476 *Journal of Geophysical Research: Atmospheres*, *112*(D17).

477 Li, W., B. L. Beard, C. Li, H. Xu, and C. M. Johnson (2015), Experimental calibration of Mg isotope fractionation
478 between dolomite and aqueous solution and its geological implications, *Geochimica et Cosmochimica Acta*, *157*, 164-
479 181.

480 Li, X., S. Huang, K. Huang, Y. Zhong, and Z. Hu (2016), Differences and controls of carbon and oxygen isotope
481 composition in dolomite and coexisting calcite under deposition conditions, *Petroleum geology and experiment*, *38*(6),
482 828-835.

483 Lippmann, F. (1974), *Sedimentary Carbonate Minerals*, Springer, Berlin, Heidelberg.

484 Liu, D., Y. Xu, D. Papineau, N. Yu, Q. Fan, X. Qiu, and H. Wang (2019), Experimental evidence for abiotic formation of
485 low-temperature proto-dolomite facilitated by clay minerals, *Geochimica et Cosmochimica Acta*, *247*, 83-95.

486 Liu, X., J. Shen, S. Wang, E. Zhang, and Y. Cai (2003), A 16 000-Year Paleoclimatic Record Derived from Authigenetic
487 Carbonate of Lacustrine Sediment in Qinghai Lake (in Chinese), *GEOLOGICAL JOURNAL OF CHINA UNIVERSITIES*,
488 *9*(1), 38-46.

489 Lu, Y., X. Sun, H. Xu, H. Konishi, Z. Lin, L. Xu, T. Chen, X. Hao, H. Lu, and J. Peckmann (2018), Formation of
490 dolomite catalyzed by sulfate-driven anaerobic oxidation of methane: Mineralogical and geochemical evidence from the
491 northern South China Sea, *American Mineralogist*, *103*(5), 720-734.

492 Lumsden, D., and G. Caudle (2001), Origin of Massive Dolostone: The Upper Knox Model, *Journal of Sedimentary*
493 *Research*, *71*.

494 Lumsden, D. N. (1979), Discrepancy between thin-section and X-ray estimates of dolomite in limestone, *Journal of*
495 *Sedimentary Research*, *49*(2), 429-435.

496 Magaritz, M., L. Goldenberg, U. Kafri, and A. Arad (1980), Dolomite formation in the seawater–freshwater interface,
497 *Nature*, *287*(5783), 622-624.

498 Marcott, S., J. Shakun, P. Clark, and A. Mix (2013), A Reconstruction of Regional and Global Temperature for the Past
499 11,300 Years, *Science*, *339*, 1198-1201.

500 McCormack, J., T. R. R. Bontognali, A. Immenhauser, and O. Kwiecien (2018), Controls on Cyclic Formation of
501 Quaternary Early Diagenetic Dolomite, *Geophysical Research Letters*, *45*(8), 3625-3634.

502 Meister, P., J. A. McKenzie, C. Vasconcelos, S. Bernasconi, M. Frank, M. Gutjahr, and D. P. Schrag (2007), Dolomite
503 formation in the dynamic deep biosphere: results from the Peru Margin, *Sedimentology*, *54*(5), 1007-1032.

504 Meng, X., L. Liu, W. Zhao, T. He, J. Chen, and J. Ji (2019), Distant Taklimakan Desert as an Important Source of
505 Aeolian Deposits on the Chinese Loess Plateau as Evidenced by Carbonate Minerals, *Geophysical Research Letters*,
506 *46*(9), 4854-4862.

507 Meng, X., L. Liu, W. Balsam, S. Li, T. He, J. Chen, and J. Ji (2015), Dolomite abundance in Chinese loess deposits: A
508 new proxy of monsoon precipitation intensity, *Geophysical Research Letters*, *42*(23).

509 Na, Q., H. Xu, D.-p. Su, M. Tao, W.-w. Zhang, Z.-p. Ji, and Q. Wang (2019), Microscopic characteristics and geological
510 significance of tight dolomite in well Xike 1, Xisha islands, China, *China Geology*, *3*(4), 459-467.

511 Ning, M., X. Lang, K. Huang, C. Li, T. Huang, H. Yuan, C. Xing, R. Yang, and B. Shen (2020), Towards understanding
512 the origin of massive dolostones, *Earth and Planetary Science Letters*, *545*.

513 Perri, E., M. E. Tucker, M. Słowakiewicz, F. Whitaker, L. Bowen, and I. D. Perrotta (2018), Carbonate and silicate
514 biomineralization in a hypersaline microbial mat (Mesaieed sabkha, Qatar): Roles of bacteria, extracellular polymeric
515 substances and viruses, *Sedimentology*, *65*(4), 1213-1245.

516 Petrash, D. A., O. M. Bialik, T. R. R. Bontognali, C. Vasconcelos, J. A. Roberts, J. A. McKenzie, and K. O. Konhauser
517 (2017), Microbially catalyzed dolomite formation: From near-surface to burial, *Earth-Science Reviews*, *171*, 558-582.

518 Pina, C. M., C. Pimentel, and Á. Crespo (2020), Dolomite cation order in the geological record, *Chemical Geology*.

519 Roberts, J. A., P. A. Kenward, D. A. Fowle, R. H. Goldstein, L. A. González, and D. S. Moore (2013), Surface chemistry
520 allows for abiotic precipitation of dolomite at low temperature, *Proceedings of the National Academy of Sciences*,
521 *110*(36), 14540.

522 Sadooni, F., F. Howari, and A. El-Saiy (2010), *Microbial dolomites from carbonate-evaporite sediments of the coastal*
523 *sabkha of Abu Dhabi and theri exploration inplication*, 289-298 pp.

524 Samylina, O. S., L. V. Zaytseva, and M. A. Sinetova (2016), Participation of algal–bacterial community in the formation
525 of modern stromatolites in Cock Soda Lake, Altai Region, *Paleontological Journal*, *50*(6), 635-645.
526 Sánchez-Román, M., J. A. McKenzie, A. de Luca Rebello Wagener, M. A. Rivadeneyra, and C. Vasconcelos (2009),
527 Presence of sulfate does not inhibit low-temperature dolomite precipitation, *Earth and Planetary Science Letters*, *285*(1),
528 131-139.
529 Sánchez-Román, M., J. A. McKenzie, A. de Luca Rebello Wagener, C. S. Romanek, A. Sánchez-Navas, and C.
530 Vasconcelos (2011), Experimentally determined biomediated Sr partition coefficient for dolomite: Significance and
531 implication for natural dolomite, *Geochimica et Cosmochimica Acta*, *75*(3), 887-904.
532 Sanz-Montero, M. E., J. P. Rodriguez-Aranda, and J. P. Calvo (2006), Mediation of Endoevaporitic Microbial
533 Communities in Early Replacement of Gypsum by Dolomite: A Case Study from Miocene Lake Deposits of the Madrid
534 Basin, Spain, *Journal of Sedimentary Research*, *76*(12), 1257-1266.
535 Shen, Z., I. Szlufarska, P. E. Brown, and H. Xu (2015), Investigation of the Role of Polysaccharide in the Dolomite
536 Growth at Low Temperature by Using Atomistic Simulations, *Langmuir*, *31*(38), 10435-10442.
537 Shinn, E. A., R. N. Ginsburg, R. M. Lloyd, L. C. Pray, and R. C. Murray (1965), Recent Supratital Dolomite from
538 Andros Island Bahamas12, in *Dolomitization and Limestone Diagenesis*, edited, p. 0, SEPM Society for Sedimentary
539 Geology.
540 Sun, F., W. Hu, X. Wang, J. Cao, B. Fu, H. Wu, and S. Yang (2020), Methanogen microfossils and methanogenesis in
541 Permian lake deposits, *Geology*.
542 Van der Meeren, T., E. Ito, D. Verschuren, J. E. Almendinger, and K. Martens (2011), Valve chemistry of Limnocythere
543 inopinata (Ostracoda) in a cold arid environment — Implications for paleolimnological interpretation, *Palaeogeography,
544 Palaeoclimatology, Palaeoecology*, *306*(3-4), 116-126.
545 Vandeginste, V., O. Snell, M. R. Hall, E. Steer, and A. Vandeginste (2019), Acceleration of dolomitization by zinc in
546 saline waters, *Nature Communications*, *10*(1), 1851.
547 Vasconcelos, C., J. A. McKenzie, S. Bernasconi, D. Grujic, and A. J. Tien (1995), *Microbial Mediation as a Possible
548 Mechanism for Natural Dolomite Formation at Low-Temperatures*, 220-222 pp.
549 Wanas, H. A., and E. Sallam (2016), Abiotically-formed, primary dolomite in the mid-Eocene lacustrine succession at
550 Gebel El-Goza El-Hamra, NE Egypt: An approach to the role of smectitic clays, *Sedimentary Geology*, *343*, 132-140.
551 Wang, J., Z. He, D. Zhu, Q. Liu, Q. Ding, S. Li, and D. Zhang (2020), Petrological and geochemical characteristics of the
552 botryoidal dolomite of Dengying Formation in the Yangtze Craton, South China: Constraints on terminal Ediacaran
553 "dolomite seas", *Sedimentary Geology*, *406*.
554 Wang, R., et al. (2018), Evolution and development of Miocene "island dolostones" on Xisha Islands, South China Sea,
555 *Marine Geology*, *406*, 142-158.
556 Wang, X., I. M. Chou, W. Hu, S. Yuan, H. Liu, Y. Wan, and X. Wang (2016), *Kinetic inhibition of dolomite
557 precipitation: Insights from Raman spectroscopy of Mg2 +–SO42 − ion pairing in MgSO4/MgCl2/NaCl solutions at
558 temperatures of 25 to 200 °C*.
559 Wang, Y., C. Wu, Y. Fang, J. Ma, B. Shen, F. Huang, L. Li, M. Ning, L. Zhai, and W. Zhang (2020), Mg, C and O
560 isotopic compositions of Late Cretaceous lacustrine dolomite and travertine in the northern Tianshan Mountains,
561 Northwest China, *Chemical Geology*, 119569.
562 Warren, J. (2000), Dolomite: occurrence, evolution and economically important associations, *Earth-Science Reviews*,
563 *52*(1), 1-81.
564 Warthmann, R., Y. Van Lith, C. Vasconcelos, J. A. Mckenzie, and A. M. Karpoff (2000), Bacterially induced dolomite
565 precipitation in anoxic culture experiments, *Geology*, *28*(12), 1091-1094.
566 Woolway, R. I., E. Jennings, T. Shatwell, M. Golub, D. C. Pierson, and S. C. Maberly (2021), Lake heatwaves under
567 climate change, *Nature*, *589*(7842), 402-407.
568 Woolway, R. I., et al. (2016), Diel Surface Temperature Range Scales with Lake Size, *PLoS One*, *11*(3), e0152466.
569 Wright, D. T. (1997), An organogenic origin for widespread dolomite in the Cambrian Eilean Dubh Formation,
570 northwestern Scotland, *Journal of Sedimentary Research*, *67*(1), 54-64.
571 Wright, D. T., and D. Wacey (2005), Precipitation of dolomite using sulphate-reducing bacteria from the Coorong
572 Region, South Australia: significance and implications, *Sedimentology*, *52*(5), 987-1008.
573 Xu, J., C. Yan, F. Zhang, H. Konishi, H. Xu, and H. H. Teng (2013), Testing the cation-hydration effect on the
574 crystallization of Ca-Mg-CO3 systems, *Proceedings of the National Academy of Sciences of the United States of
575 America*, *110*(44), 17750-17755.
576 Yancheva, G., N. R. Nowaczyk, J. Mingram, P. Dulski, G. Schettler, J. F. Negendank, J. Liu, D. M. Sigman, L. C.
577 Peterson, and G. H. Haug (2007), Influence of the intertropical convergence zone on the East Asian monsoon, *Nature*,
578 *445*(7123), 74-77.
579 Yang, J., J. Chen, Z. An, G. Shields-Zhou, X. Tao, H. Zhu, J. Ji, and Y. Chen (2000), Variations in 87Sr/86Sr ratios of
580 calcites in Chinese loess: A proxy for chemical weathering associated with the East Asian summer monsoon,
581 *Palaeogeography Palaeoclimatology Palaeoecology - PALAEOGEOGR PALAEOCLIMATOL*, *157*, 151-159.
582 Zhang, D., and Z. Feng (2018), Holocene climate variations in the Altai Mountains and the surrounding areas: A
583 synthesis of pollen records, *Earth-Science Reviews*, *185*, 847-869.

584 Zhang, F., H. Xu, H. Konishi, E. S. Shelobolina, and E. E. Roden (2012), Polysaccharide-catalyzed nucleation and
585 growth of disordered dolomite: A potential precursor of sedimentary dolomite, *American Mineralogist*, *97*(4), 556-567.
586 Zhang, F., H. Xu, E. S. Shelobolina, H. Konishi, B. Converse, Z. Shen, and E. E. Roden (2015), The catalytic effect of
587 bound extracellular polymeric substances excreted by anaerobic microorganisms on Ca-Mg carbonate precipitation:
588 Implications for the "dolomite problem", *American Mineralogist*, *100*(2-3), 483-494.
589 Zhao, J., C.-B. An, Y. Huang, C. Morrill, and F.-H. Chen (2017), Contrasting early Holocene temperature variations
590 between monsoonal East Asia and westerly dominated Central Asia, *Quaternary Science Reviews*, *178*, 14-23.
591
592